IEEE Access
Multidisciplinary ⋮ Rapid Review ⋮ Open Access Journal

Received 3 September 2023, accepted 11 October 2023, date of publication 16 October 2023, date of current version 23 October 2023.

Digital Object Identifier 10.1109/ACCESS.2023.3324918

RESEARCH ARTICLE

Global Sensitivity Analysis in Aerodynamic Design Using Shapley Effects and Polynomial Chaos Regression

PRAMUDITA SATRIA PALAR[1], LAVI RIZKI ZUHAL[1], AND KOJI SHIMOYAMA[2], (Member, IEEE)

[1]Faculty of Mechanical and Aerospace Engineering, Bandung Institute of Technology, Bandung, West Java 40132, Indonesia
[2]Department of Mechanical Engineering, Kyushu University, Fukuoka 819-0395, Japan

Corresponding author: Pramudita Satria Palar (pramsp@itb.ac.id)

The work of Pramudita Satria Palar and Lavi Rizki Zuhal was supported by Institut Teknologi Bandung through the P2MI 2023 Program.

ABSTRACT Quantifying the impact of design variables in aerodynamic design exploration can provide valuable insights to designers. Global sensitivity analysis (GSA) is a crucial tool in aerodynamic design exploration that enables designers to gain valuable insights by quantifying the impact of design variables. In the field of GSA, the Shapley effect is a powerful alternative to total Sobol indices due to several mathematical advantages of the former. However, computing the Shapley effect is computationally expensive due to the large number of permutations involved. To overcome this challenge, surrogate models are often used to accurately estimate Shapley effects while reducing the number of function calls. This paper aims to investigate the effectiveness of using PCE to compute Shapley effects for independent inputs in aerodynamic design exploration. The exact calculation from PCE also enables the rapid assessment of confidence intervals for Shapley effects, taking into account the randomness in the experimental design via bootstrap resampling. The usefulness of Shapley effects with PCE is then demonstrated and compared with total Sobol indices through a nonlinear test function and three engineering problems, including subsonic wing, transonic airfoil, and fan blade design. The results also show that the confidence intervals of the Shapley effects are narrower than those of total Sobol indices, allowing better interpretation and higher confidence on the estimated GSA metric.

INDEX TERMS Global sensitivity analysis, Shapley effects, polynomial chaos expansion, aerodynamics.

I. INTRODUCTION

Assessing the relative importance of input variables to the output of interest is crucial, and Global Sensitivity Analysis (GSA) plays a significant role in this regard. In design exploration, GSA provides essential information on which design variables have the most significant impact on the objective function. This helps engineers focus their attention on these variables and make informed design decisions, in which such a framework was first investigated in the context of aerodynamic optimization by Obayashi et al. [1], [2], who applied GSA to investigate the impact of geometrical variables on aerodynamic performances of flying vehicles. GSA is a useful tool in uncertainty quantification that identifies the contribution of individual random inputs and their interactions that affect the random output. This analysis allows for both quantitative and intuitive assessment of the influence of multiple input random variables on the random output in the context of uncertainty analysis. GSA provides distinct information compared to local sensitivity analysis, which offers local sensitivity via gradient information. Variance-based sensitivity analysis [3] is arguably the most popular form of GSA due to its intuitive concept: the output variance is decomposed into individual components so that they correspond to the contribution of the input variables. Alternatives of the GSA metric include derivative-based

The associate editor coordinating the review of this manuscript and approving it for publication was Rosario Pecora.

global sensitivity measures [4] and activity scores based on active subspace [5]. Typically, a Monte Carlo simulation (MCS) is used to compute GSA metrics.

A natural approach to perform GSA when the computer simulation is expensive is to replace the actual function with a surrogate model. Surrogate models significantly reduce the number of computer simulation calls compared to a crude MCS. Instead, the MCS calls the surrogate model to estimate the sensitivity indices in place of the black-box simulation. Various surrogate models have been applied for GSA, including radial basis functions [6], Kriging/Gaussian process regression [7], [8], support vector regression [9], [10], random forest [11], and polynomial chaos expansion (PCE) [12], [13]; for most of the papers in surrogate-based GSA, Sobol indices [14] is the most widely used GSA method. Another possibility is to deploy a neural network as an approximation model [15], [16]. PCE is especially advantageous for GSA since the estimated Sobol indices can be exactly computed from the PCE coefficients [12]. PCE is also suitable for high-dimensional problems by introducing sparse algorithms to seek the best polynomial subset that minimizes approximation error (see [17] for a recent review of sparse PCE). A comparison of various surrogate models in analytical problems for GSA has been performed by Cheng et al. [18].

GSA plays an important role in aerodynamic design optimization and uncertainty quantification. Identifying the significance of input variables (design or random variables) on the performance can greatly aid designers in understanding the design landscape of an aerodynamic design problem. Some recent examples include identifying the most impactful geometrical design variables for aerodynamic optimization of delaying airfoil dynamic stall using Kriging and Sobol indices [19]. Fan et al. use a surrogate model and GSA to investigate the impact of ducted-fan rotor geometry on its aerodynamic and structural performance [20]. Another example is the design optimization of scramjet engines [21], in which the authors successfully identified via GSA that injection pressure is the most significant variable, contributing to roughly 70% on thrust among the four design variables. Recently, Siddique and Raj applied radial basis function surrogate and Sobol indices to analyze the sensitivity of aerodynamic performances [22]. The overarching idea is that pinpointing the most influential variables can provide valuable insights into the aerodynamic design problem at hand. Similarly, GSA also helps aerodynamic designers in identifying the most significant random input variables to provide information on how to reduce the variance of the aerodynamic performance, e.g., due to variable operating conditions or modeling parameters in high-altitude propellers [23], turbomachinery [24], transonic airfoil [25], and hypersonic vehicles [26]

It is common to use total Sobol indices to quantify the overall effect of input variables on the output function. The total Sobol index for one variable is calculated by summing out the main effect and all the interaction terms which include that variable. The total Sobol indices of all variables are then ordered to rank the input variables based on their importance. Sobol indices have demonstrated favourable performance when the sample size is adequately large [27]. However, one problem with total Sobol indices is that they somehow lose their intuitiveness because the sum of total Sobol indices is not equal to one. One remedy is by introducing the Shapley effect [28], [29], which is based on the Shapley values from game theory. In contrast to Sobol indices, the Shapley effect allocates a variable's contribution due to the main effect and interactions more fairly. Calculation of Shapley effects is notably more expensive than the Sobol indices due to the large number of permutations that need to be considered. Shapley effect is more favourable and interpretable than total Sobol indices in problems with dependent inputs [30]. However, Shapley effects and total Sobol indices can produce different importance rankings even when the inputs are independent since the sum of all Shapley effects equals the total variance. A simple and efficient algorithm for calculating Shapley effects with independent inputs has been proposed [31]. The use of Kriging for estimation of Shapley values in computationally expensive problems has also been studied [32].

Polynomial chaos expansion (PCE) [33], [34] has been widely applied for GSA, thanks to its rapid model construction and the availability of analytical forms for some global sensitivity indices, including Sobol indices [12] and derivative-based global sensitivity measures [35]. In this respect, the analytical estimation of global sensitivity indices, especially Sobol indices, proves helpful because there is no further need to apply MCS on the surrogate model. Thus, PCE completely eliminates the uncertainty due to random sampling on the surrogate model. The PCE technique has also been extended to take into account multi-fidelity information for GSA [36]. PCE uses orthogonal polynomials from the Askey scheme as the basis function. However, arbitrary input distributions can be handled by arbitrary polynomial chaos or even purely data-driven [37], [38]. Because non-intrusive PCE is a surrogate model, any global sensitivity measure can be estimated by applying MCS on PCE. However, the use of MCS introduces extra uncertainty to the estimation.

The focus of our research is to examine the utilization of PCE as a means of estimating Shapley effects for aerodynamic functions with independent input variables. The non-intrusive nature of PCE makes it an attractive choice for a surrogate model, as it can be constructed relatively quickly compared to other methods like Gaussian Processes Regression. One of the most significant advantages of PCE is that the Shapley effects for independent input variables can be computed analytically from the PCE coefficients. This feature enables us to eliminate uncertainties caused by random sampling in MCS and reduce the problem of computing Shapley effects of a PCE model by simply post-processing the PCE coefficients. In this paper, we present the benefits

of this approach through numerical experiments conducted on various aerodynamic test functions, especially those with strong interactions. Additionally, some test problems demonstrate a different variable ranking based on the total Sobol indices and Shapley effects. Finally, we also show how a bootstrap procedure can be utilized to construct a confidence interval for the Shapley effects estimated from a PCE model, similar to the approach in [39].

The contributions of this paper are then twofold: (1) the exact calculation of Shapley effects from a PCE model which eliminates the use of Monte Carlo simulation, and (2) the comparison of Shapley effect and total Sobol indices for GSA of aerodynamic problems, particularly those with strong interactions, from the viewpoint of variable ranking and bootstrap confidence interval. The insight obtained from this research will be useful for those who wish to perform GSA, especially when faced with computational budget constraints and a desire for efficient, data-driven decision-making in aerodynamic design processes.

Section II describes the Shapley Effects for GSA. Section III describes the PCE model and the fast analytical estimation of Shapley effects from PCE. Section IV shows the numerical experiment results on aerodynamic problems and the discussion. Finally, we conclude the paper in Section V with pointers for future works.

II. SHAPLEY EFFECTS

Let us define a vector of input variables $\boldsymbol{\xi} = \{\xi_1, \xi_2, \ldots, \xi_m\}^T \in \mathbb{R}^m$, where $m \geq 1$ is the dimensionality of the input variables. Each input variable ξ_i is equipped with a probability distribution $\rho_{\xi_i}(\xi_i)$. We assume that the random input variables are independent; thus, we have $\rho(\boldsymbol{\xi}) = \prod_{i=1}^{m} \rho_{\xi_i}(\xi_i)$ as the joint probability density function (PDF). We also define the domain of interest as $\Omega = \prod_{i=1}^{m} \Omega_i$. For more compact explanations, we shall use the following notations. First, we use $[1:m] := \{1, \ldots, m\}$ and we also define a subset of $[1:m]$ as u (i.e., $u \subseteq [1:m]$), $\{-u\}$ is the complement of u such that $\{-u\} = [1:m] \setminus u$, and $|u|$ is the cardinality of u. The subset of Ω for an index set u is defined as $\Omega_u = \prod_{i \in u} \Omega_i$ with the corresponding PDF is $\rho_u(\boldsymbol{\xi}_u) = \prod_{i \in u} \rho_{\xi_i}(\xi_i)$. It is important to note that we have expressed the probability density function and the domain for $u = [1:m]$ as $\rho(\boldsymbol{\xi})$ and Ω, respectively.

Let us also define a function $y = f(\boldsymbol{\xi})$ which takes $\boldsymbol{\xi}$ as the input. The function $f(\boldsymbol{\xi})$ is square-integrable in Ω, that is, $\int_\Omega f^2(\boldsymbol{\xi})\rho(\boldsymbol{\xi})d\boldsymbol{\xi}$ yields a finite value. It is important to note that when dealing with bounded problems without any probability measure (such as in optimization problems), the approach is similar to that of handling a uniform probability distribution.

A. ANOVA DECOMPOSITION

By utilizing the ANOVA decomposition, it is possible to break down a function $f(\boldsymbol{\xi})$ into its constituent parts, including the main effects of individual variables as well as the interactions between multiple variables. This allows for a more thorough analysis of the function and its underlying components, written as

$$y = f(\boldsymbol{\xi}) = \sum_{u \subseteq [1:m]} f_u(\boldsymbol{\xi}_u), \tag{1}$$

which consists of the following summand:

$$f_\emptyset = \int_\Omega f(\boldsymbol{\xi})\rho(\boldsymbol{\xi})d\boldsymbol{\xi} = \mathbb{E}[f(\boldsymbol{\xi})] \tag{2}$$

which is the mean of $f(\boldsymbol{\xi})$ and

$$f_u(\boldsymbol{\xi}_u) = \int_{\Omega_{-u}} f(\boldsymbol{\xi})\rho(\boldsymbol{\xi}_{-u})(\boldsymbol{\xi}_{-u})d\boldsymbol{\xi}_{-u} - \sum_{v \not\subseteq u} f_v(\boldsymbol{\xi}_v), \tag{3}$$

for a non-empty subset u, where the subscript $-u$ again indicates "complement of u". For example,

$$f_i(\xi_i) = \mathbb{E}[f(\boldsymbol{\xi})|\xi_i] - f_0, \tag{4}$$

$$f_{i,j}(\xi_i, \xi_j) = \mathbb{E}[f(\boldsymbol{\xi})|\xi_i, \xi_j] - f_0 - f_i - f_j. \tag{5}$$

The $f_i(\xi_i)$ term is known as the main effect, which is obtained by varying ξ_i alone. On the other hand, the higher-order terms are known as interactions. For example, $f_{i,j}(\xi_i, \xi_j)$ is the effect of simultaneously varying ξ_i and ξ_j.

For a non-empty subset u (i.e., excluding $f_\emptyset$) and $j \in u$, the following orthogonality condition applies

$$\int_\Omega f_u(\boldsymbol{\xi}_u) f_v(\boldsymbol{\xi}_v)\rho(\boldsymbol{\xi})d\boldsymbol{\xi} = \begin{cases} \sigma_u^2 := \int_{\Omega_u} (f_u(\boldsymbol{\xi}_u))^2 \rho_u(\boldsymbol{\xi}_u)d\boldsymbol{\xi}_u & \text{if } u = v \\ 0 & \text{otherwise} \end{cases} \tag{6}$$

for any $u, v \subseteq [1:m]$

Because $f(\boldsymbol{\xi})$ is square-integrable, we can obtain the variance of $f(\boldsymbol{\xi})$ (i.e., $\mathbb{V}[f(\boldsymbol{\xi})]$) by

$$\int_\Omega (f(\boldsymbol{\xi}) - f_\emptyset)^2 \rho(\boldsymbol{\xi})d\boldsymbol{\xi} = \mathbb{V}[f(\boldsymbol{\xi})] = \int_\Omega \left(\sum_{\emptyset \neq u \subseteq [1:m]} f_u(\boldsymbol{\xi}_u) \right)^2 \rho(\boldsymbol{\xi})d\boldsymbol{\xi} = \sum_{\emptyset \neq u \subseteq [1:m]} V_u \tag{7}$$

where V_u is called partial variance, which is defined as

$$V_u = \mathbb{V}[f_u(\boldsymbol{\xi}_u)] = \sigma_u^2. \tag{8}$$

Basically, Eq. (7) says that the sum of all partial variances equals the total variance.

The main effect is defined as V_i, reads as

$$V_i \equiv \mathbb{V}[f_i(\xi_i)] \equiv \mathbb{V}[\mathbb{E}[f(\boldsymbol{\xi})|\xi_i]] = \mathbb{V}[f(\boldsymbol{\xi})] - \mathbb{E}[\mathbb{V}[f(\boldsymbol{\xi})|\xi_i]]. \tag{9}$$

On the other hand, the total effect is defined as

$$V_{T_i} = \sum_{u \in \Xi_i} V_u \tag{10}$$

where $\Xi_i = \{(i_1, \ldots, i_{|u|}) : \exists j, 1 \leq j \leq |u|, i_j = i\}$ and $\Xi_i \subseteq [1:m]$. The total effect for variable i sums the main effect and all interaction terms that contain variable i.

For simplicity, we denote the total variable $\mathbb{V}[f(\boldsymbol{\xi})]$ as simply V. The Sobol indices for a non-empty subset u can then be defined as

$$S_u = \frac{V_u}{V}. \tag{11}$$

Thus, we have the widely used total Sobol indices defined as follows

$$S_{T_i} = \frac{V_{T_i}}{V}, \tag{12}$$

where $i = 1, 2, \ldots, m$. Although total Sobol indices are popular, their main drawback is that the sum of total Sobol indices can be higher than one (i.e., $\sum_{i=1}^{m} S_{T_i} \geq 1$ since $\sum_{i=1}^{m} V_{T_i} \geq V$). Using S_{T_i} is a viable option for assessing the significance of input variables. However, in cases where there are strong interactions between variables, there is a high risk of misinterpretation, making it challenging to grasp the input variables' relative impact on the output.

B. DEFINITION OF SHAPLEY EFFECT

Shapley effect is proposed by Owen [28] to remedy the normalization problem in total and first-order Sobol indices. Unlike V_{T_i}, the sum of Shapley effect ϕ equals to the total variance, i.e., $\sum_{i=1}^{m} \phi_i = V$, which allows easier interpretation in the context of GSA. Shapley effect is a special case of Shapley value from game theory by assigning a special value function in the formulation.

The Shapley value for the i-th individual variable is defined by

$$\phi_i = \frac{1}{m} \sum_{u \subseteq \{-i\}} \binom{m-1}{|u|}^{-1} (\text{val}(u \cup \{i\}) - \text{val}(u)), \tag{13}$$

where val(.) is the value function assigned to the subset defined inside the bracket.

In the context of GSA, the necessary conditions for val(.) are $\text{val}(\emptyset) = 0$ and $\text{val}([1 : m]) = \mathbb{V}[f(\boldsymbol{\xi})]$. That is, the variance for an empty set and with all variables included equal 0 and the total variance, respectively. We can use the following value function to satisfy the aforementioned two conditions:

$$\text{val}(u) = \tau(u) = \mathbb{V}[\mathbb{E}(f(\boldsymbol{\xi})|\boldsymbol{\xi}_u)] = \sum_{\emptyset \neq v \subseteq u} V_v. \tag{14}$$

The $\tau(u)$ is interpreted as the expected reduction of the overall variance when $\boldsymbol{\xi}_u$ is known. Thus, $\tau(\emptyset) = 0$ and $\tau([1 : m]) = \mathbb{V}[f(\boldsymbol{\xi})]$. Notice that $\tau(u)$ is not simply V_u, but it is the sum of all possible V_v where $v \subseteq u$. However, for a singleton $\tau(\{j\})$, $\tau(u)$ equals the partial variance V_u. Alternatively, the following value function can also be used:

$$\text{val}(u) = \bar{\tau}(u) = \mathbb{E}[\mathbb{V}(f(\boldsymbol{\xi})|\boldsymbol{\xi}_{\bar{u}}], \tag{15}$$

where $\bar{u} = [1 : d] \setminus u$.

Thus, by using $\tau(u)$ as the value function, the Shapley effect can be calculated as follows

$$\phi_i = \frac{1}{m} \sum_{u \subseteq \{-i\}} \binom{m-1}{|u|}^{-1} (\tau(u \cup \{i\}) - \tau(u)), \tag{16}$$

The appealing point of the Shapley effect is that the sum of all Shapley effects equals the total variance V, that is

$$\sum_{i=1}^{m} \phi_i = V. \tag{17}$$

For easier interpretation, we denote $\tilde{\phi}_i$ as ϕ_i / V. Hence,

$$\sum_{i=1}^{m} \tilde{\phi}_i \equiv \sum_{i=1}^{m} \frac{\phi_i}{V} = 1. \tag{18}$$

Based on this equation, we can conclude that the Shapley effect is a more rational approach for gauging the significance of input variables, unlike total Sobol indices. As evidenced by some of the test problems presented in this paper, the rankings of input variable importance can differ between Shapley effects and total Sobol indices.

For illustration, consider a problem with three input variables $\boldsymbol{\xi} = \{\xi_1, \xi_2, \xi_3\}^T$. By applying Eq. (16), the Shapley effect for ξ_1 can be written as

$$\begin{aligned}\phi_1 = {} & \frac{1}{3}\tau_{\{1\}} + \frac{1}{6}\left[(\tau_{\{1,2\}} - \tau_{\{2\}}) + (\tau_{\{1,3\}} - \tau_{\{3\}})\right] \\ & + \frac{1}{3}(\tau_{\{1,2,3\}} - \tau_{\{2,3\}}),\end{aligned} \tag{19}$$

which eventually yields

$$\phi_1 = V_1 + \frac{1}{2}V_{1,2} + \frac{1}{2}V_{1,3} + \frac{1}{3}V_{1,2,3}. \tag{20}$$

There are various ways to calculate Shapley effects for independent variables, including using random sampling algorithms. One recent algorithm for computing Shapley effects is Goda's method, which also provides a confidence interval that is vital for further assessment, as described in [31]. However, random sampling methods may not be practical for computationally intensive problems. In such cases, surrogate models can be substituted for the black-box function to estimate Shapley effects. For example, Kriging models have been employed in prior studies to compute Shapley effects, as illustrated in [32]. This paper concentrates on PCE as Shapley effects for independent variables can be precisely calculated from the coefficients, as demonstrated later on.

III. POLYNOMIAL CHAOS EXPANSION

A. NON-INTRUSIVE PCE

The non-intrusive PCE estimates a black-box function $f(\boldsymbol{\xi})$ by expanding it using orthogonal polynomials:

$$f(\boldsymbol{\xi}) \approx \hat{f}(\boldsymbol{\xi}) = \sum_{\boldsymbol{\Gamma} \in \mathcal{K}_p} \alpha_{\boldsymbol{\Gamma}} \Psi_{\boldsymbol{\Gamma}}(\boldsymbol{\xi}) \tag{21}$$

where $\boldsymbol{\alpha}$ are the PCE coefficients, Ψ are multivariate orthogonal polynomials, $\boldsymbol{\Gamma} = \{\gamma_1, \gamma_2, \ldots, \gamma_m\}$, where $\gamma_i \geq 0$ for $i = 1, 2, \ldots$ is an index set which is part of an index set $\mathcal{K}_p$. A multivariate orthogonal polynomial $\Psi_{\boldsymbol{\Gamma}}$

is constructed as the tensor product of univariate orthogonal polynomials $\psi_{\gamma_i}^{(i)}$, where $i = 1, \ldots, m$:

$$\Psi_{\boldsymbol{\Gamma}} = \prod_{i=1}^{m} \psi_{\gamma_i}^{(i)}(\xi_i) \tag{22}$$

PCE uses an expansion of polynomials which are orthogonal in the following sense:

$$\langle \Psi_i(\boldsymbol{\xi}) \Psi_j(\boldsymbol{\xi}) \rangle = \int_{\Omega} \Psi_i(\boldsymbol{\xi}) \Psi_j(\boldsymbol{\xi}) \rho(\boldsymbol{\xi}) d\boldsymbol{\xi} = \delta_{ij}, \tag{23}$$

where $\delta_{ij} = 1$ if $i = j$ and 0 if $i \neq j$. There exists a polynomial family that satisfies the orthonormality constraints corresponding to the given input probability distribution. For example, Hermite and Legendre polynomials are used for normal and uniform distribution, respectively [33].

In this paper, the index set $\mathcal{K}_p$ is generated by using a total-order expansion of order p, as defined by

$$\mathcal{K}_p \equiv \{\boldsymbol{\Gamma} \in \mathbb{N}^m : |\boldsymbol{\Gamma}| \leq p\}. \tag{24}$$

To reduce the size of the polynomial basis set, it is also common to use hyperbolic truncation which takes an extra parameter q such that

$$\mathcal{K}_p \equiv \{\boldsymbol{\Gamma} \in \mathbb{N}^m : |\boldsymbol{\Gamma}|_q \leq p\}, \tag{25}$$

where

$$|\boldsymbol{\Gamma}|_q = \left(\sum_{i=1}^{m} \alpha_i^q \right)^{1/q}. \tag{26}$$

The regression approach calculates the coefficients by minimizing the error between the PCE and the data. To use the regression approach, one collects an experimental design consisting of n samples $\mathcal{X} = \{\boldsymbol{\xi}^{(1)}, \ldots, \boldsymbol{\xi}^{(n)}\}^T$ and the responses $\boldsymbol{y} = \{y^{(1)}, \ldots, y^{(n)}\}^T = \{f(\boldsymbol{\xi}^{(1)}), \ldots, f(\boldsymbol{\xi}^{(n)})\}^T$. The coefficients $\boldsymbol{\alpha}$ are obtained by solving the following system of linear equations:

$$\boldsymbol{F}\boldsymbol{\alpha} = \boldsymbol{y} \tag{27}$$

where $\boldsymbol{F}$ is a regression matrix constructed from $\mathcal{X}$ and the index set $\mathcal{K}_p$, with its (i, j) component is $F_{ij} = \Psi_j(\boldsymbol{\xi}^{(i)})$. By defining $P = |\mathcal{K}_p|$ as the cardinality of the index set, the size of $\boldsymbol{F}$ and $\boldsymbol{\alpha}$ are then $n \times P$ and $P \times 1$, respectively. We use sparse PCE based on least-angle regression (LAR) [40] so that we can set $P > n$. The sparse algorithm will give zeros to less important terms so that the number of non-zero terms is less than n.

Rewriting the PCE as a sum of the truncated set, we have the following:

$$f(\boldsymbol{\xi}) = \hat{f}(\boldsymbol{\xi}) + \varepsilon = \sum_{j=0}^{P-1} \alpha_j \Psi_j(\boldsymbol{\xi}) + \varepsilon \equiv \boldsymbol{\alpha}^T \boldsymbol{\Psi}(\boldsymbol{\xi}) + \varepsilon \tag{28}$$

where ε is the residual. The LAR algorithm aims to find the best subset so as to yield the lowest penalized mean square error:

$$\hat{\boldsymbol{\alpha}} = \arg\min \mathbb{E}\left[(\boldsymbol{\alpha}^T \boldsymbol{\Psi}(\boldsymbol{\xi}) - f(\boldsymbol{\xi}))^2 \right] + \lambda ||\boldsymbol{\alpha}||_1, \tag{29}$$

where the purpose of the regularization term λ and $||\boldsymbol{\alpha}||_1$ is to enforce sparsity of the polynomial bases. The choice of L1 norm drives the coefficients of less influential factors to be precisely zero, thereby encouraging sparsity. The importance of sparsity becomes evident when working with high-dimensional problems, as it simplifies the process of least squares. This contrasts the L2 norm, which diminishes coefficients but does not force them to be exactly zero. To minimize the error term, the leave-one-out cross-validation (LOOCV) is used, and an analytical formulation is available for computing LOOCV error (ϵ_{LOO}) using PCE. This enables quick scanning of a vast array of basis subsets, thanks to the rapid estimation of LOOCV error. Further information on PCE with the LAR algorithm is available in [40]. It should be noted that although we used LAR, other non-intrusive PCE building methods such as spectral projection or other sparse algorithms (as described in [17]) can be utilized.

The root-mean-squared error (RMSE) is to estimate the error of the PCE model, written as

$$\epsilon_{RMSE} = \sqrt{\frac{1}{n_v} \sum_{i=1}^{n_v} \left(f(\boldsymbol{\xi}^{(i)}) - \hat{f}(\boldsymbol{\xi}^{(i)}) \right)^2}, \tag{30}$$

where n_v is the size of validation samples, $f(\boldsymbol{\xi}^{(i)})$ is the actual response, and $\hat{f}(\boldsymbol{\xi}^{(i)})$ is the PCE prediction. The LOOCV error, on the other hand, is computed as follows:

$$\epsilon_{LOO} = \sqrt{\frac{1}{n} \sum_{i=1}^{n} \left(f(\boldsymbol{\xi}^{(i)}) - \hat{f}^{(-i)}(\boldsymbol{\xi}^{(i)}) \right)^2}, \tag{31}$$

where $\hat{f}^{(-i)}(\boldsymbol{\xi}^{(i)})$ is the PCE prediction constructed from a reduced experimental design by removing the i-th sample (hence, the name leave-one-out). To ease the analysis, the errors are normalized according to the interquartile range of the responses estimated from all available samples.

B. SHAPLEY EFFECTS FROM PCE

As the non-intrusive PCE is essentially a surrogate model, the most straightforward approach for calculating Shapley effects from a PCE model is to use a random sampling-based algorithm or Monte Carlo sampling. Song et al. proposed a Monte Carlo algorithm [29] that is general and can be used for both independent and dependent inputs. One of the latest methods for computing Shapley effects with smaller confidence intervals for independent inputs is Goda's algorithm [31]. However, exact computation of PCE-based Shapley effects can be advantageous because it enables even faster computation. Furthermore, exact computation eliminates the need for confidence intervals since no random sampling is involved.

The orthogonality of the polynomial terms in PCE is particularly useful because the PCE can be conveniently decomposed according to the Sobol decomposition. It is advantageous that the Shapley effects from the constructed

PCE model can also be obtained exactly from the PCE coefficients.

First, it is known that $\mathbb{E}[f(\boldsymbol{\xi})] = \alpha_0$ due to orthogonality of the PCE basis. Hence, we have the variance of PCE (i.e., V^{PC}) as follows:

$$V^{PC} = \sigma^2_{PC} = \mathbb{V}\left[\sum_{j=0}^{P-1} \alpha_j \Psi_j(\boldsymbol{\xi})\right] = \mathbb{E}\left[\left(\sum_{j=1}^{P-1} \alpha_j \Psi_j(\boldsymbol{\xi}) - \alpha_0\right)^2\right] = \sum_{j=1}^{P-1} \alpha_j^2 \mathbb{E}[\Psi_j^2(\boldsymbol{\xi})]. \tag{32}$$

Because $\mathbb{E}[\Psi_j^2(\boldsymbol{\xi})] = 1$ due to the orthonormality of the bases, for any j, we have

$$V^{PC} = \sum_{j=1}^{P-1} \alpha_j^2 \tag{33}$$

Obtaining V^{PC} is particularly important when using the normalized version of Shapley effects. Let us first define $\mathcal{L}_u$ as the set of $\boldsymbol{\Gamma}$ tuples such that

$$\mathcal{L}_u = \left\{ \boldsymbol{\Gamma} : \begin{matrix} \gamma_k > 0 \ \forall k = 1, \ldots, m \ k \in u \\ \gamma_k = 0 \ \forall k = 1, \ldots, m \ k \notin u \end{matrix} \right\} \tag{34}$$

We can then write

$$\hat{f}_u(\boldsymbol{\xi}_u) = \sum_{\boldsymbol{\Gamma} \in \mathcal{L}_u} \boldsymbol{\alpha}_{\boldsymbol{\Gamma}} \boldsymbol{\Psi}_{\boldsymbol{\Gamma}}(\boldsymbol{\xi}_u), \tag{35}$$

as the summand in the ANOVA decomposition of PCE that essentially collects all polynomials that depend only on u. The partial variance V_u^{PC} of a PCE model can then be written as

$$V_u^{PC} = \sum_{\boldsymbol{\Gamma} \in \mathcal{L}_u} \boldsymbol{\alpha}^2_{\boldsymbol{\Gamma}} \mathbb{E}[\boldsymbol{\Psi}^2_{\boldsymbol{\Gamma}}(\boldsymbol{\xi}_u)] \tag{36}$$

The Shapley effect for ξ_i, where $i \in \{1, \ldots, m\}$, for independent inputs can be calculated as

$$\phi_i = \sum_{\emptyset \neq u \subseteq [1:m], i \in u} \frac{V_u}{|u|} \tag{37}$$

Finally, the Shapley effect ϕ_i from a PCE model can then be defined as

$$\phi_i^{PC} = \sum_{\emptyset \neq u \subseteq [1:m], i \in u} \left(\frac{1}{|u|} \sum_{\boldsymbol{\Gamma} \in \mathcal{L}_u} \boldsymbol{\alpha}^2_{\boldsymbol{\Gamma}} \mathbb{E}[\boldsymbol{\Psi}^2_{\boldsymbol{\Gamma}}(\boldsymbol{\xi}_u)] \right) \tag{38}$$

Eq. (38) simply says the Shapley effect of a PCE model for any independent input variable can be computed simply from the coefficients. To summarize: (1) firstly, collect all terms u that has i as their member (2) secondly, for all admissible u, gather all polynomials that belong to $\mathcal{L}_u$, (3) square and sum all the corresponding coefficients and divide it by the cardinality of u, and, finally (4) sum the terms inside the bracket for all admissible u.

Lastly, because V^{PC} is also exactly computed, the normalized Shapley effects of a PCE model is simply written as

$$\tilde{\phi}_i^{PC} = \frac{\phi_i^{PC}}{V^{PC}}. \tag{39}$$

For example, consider approximating a three-dimensional problem with a PCE model with the following terms: $\hat{f}(\boldsymbol{\xi}) = \sum_{i=0}^{10} \alpha_j \Psi_j(\boldsymbol{\xi})$, created from a total order expansion of order $p = 3$ with the addition of the third-level interaction. Thus, we have the following set of orthogonal polynomials

$$\begin{aligned}
\Psi_0(\boldsymbol{\xi}) &= \psi_0(\xi_1)\psi_0(\xi_2)\psi_0(\xi_3) \\
\Psi_1(\boldsymbol{\xi}) &= \psi_1(\xi_1)\psi_0(\xi_2)\psi_0(\xi_3) \\
\Psi_2(\boldsymbol{\xi}) &= \psi_0(\xi_1)\psi_1(\xi_2)\psi_0(\xi_3) \\
\Psi_3(\boldsymbol{\xi}) &= \psi_0(\xi_1)\psi_0(\xi_2)\psi_1(\xi_3) \\
\Psi_4(\boldsymbol{\xi}) &= \psi_2(\xi_1)\psi_0(\xi_2)\psi_0(\xi_3) \\
\Psi_5(\boldsymbol{\xi}) &= \psi_1(\xi_1)\psi_1(\xi_2)\psi_0(\xi_3) \\
\Psi_6(\boldsymbol{\xi}) &= \psi_1(\xi_1)\psi_0(\xi_2)\psi_1(\xi_3) \\
\Psi_7(\boldsymbol{\xi}) &= \psi_0(\xi_1)\psi_2(\xi_2)\psi_0(\xi_3) \\
\Psi_8(\boldsymbol{\xi}) &= \psi_0(\xi_1)\psi_1(\xi_2)\psi_1(\xi_3) \\
\Psi_9(\boldsymbol{\xi}) &= \psi_0(\xi_1)\psi_0(\xi_2)\psi_2(\xi_3) \\
\Psi_{10}(\boldsymbol{\xi}) &= \psi_1(\xi_1)\psi_1(\xi_2)\psi_1(\xi_3)
\end{aligned}$$

with $\boldsymbol{\alpha} = \{\alpha_0, \alpha_1, \ldots, \alpha_{10}\}^T$. It is worth noting that $\psi_0 = 1$ for any input variable. We can then calculate the Shapley effect for ξ_1 by looking at the terms where the order of the PCE basis for ξ_1 is not zero, which leaves us with $\Psi_1(\boldsymbol{\xi})$, $\Psi_4(\boldsymbol{\xi})$, $\Psi_5(\boldsymbol{\xi})$, $\Psi_6(\boldsymbol{\xi})$ and $\Psi_{10}(\boldsymbol{\xi})$. We can easily calculate the Shapley effects as follows

$$V^{PC}\tilde{\phi}_1^{PC} = (\alpha_1^2 + \alpha_4^2) + \frac{1}{2}\alpha_5^2 + \frac{1}{2}\alpha_6^2 + \frac{1}{3}\alpha_{10}^2. \tag{40}$$

Similarly, for ξ_2 and ξ_3 we, respectively, have

$$V^{PC}\tilde{\phi}_2^{PC} = (\alpha_2^2 + \alpha_7^2) + \frac{1}{2}\alpha_5^2 + \frac{1}{2}\alpha_8^2 + \frac{1}{3}\alpha_{10}^2 \tag{41}$$

and

$$V^{PC}\tilde{\phi}_3^{PC} = (\alpha_3^2 + \alpha_9^2) + \frac{1}{2}\alpha_6^2 + \frac{1}{2}\alpha_8^2 + \frac{1}{3}\alpha_{10}^2. \tag{42}$$

The concept is the same for higher-dimensional inputs and higher order PCE basis. It is worth noting again that not all interaction terms would exist if a sparse PCE is used.

C. USING BOOTSTRAP FOR BUILDING CONFIDENCE INTERVAL

As PCE approximates the original model, there may be a discrepancy between the Shapley effects of the original function and those obtained through PCE. To inform analysts about the uncertainty of the estimations, it is crucial to provide a confidence interval for the PCE-based Shapley effects due to metamodeling error. One benefit of the exact calculation of Shapley effects from PCE is that it can expedite the bootstrapping process. Bootstrapping is

a valuable technique that enables quantification of the confidence interval in estimated Shapley effects. It functions by generating bootstrap samples, each containing a subset of the experimental design created from sampling with replacement. It is important to note that bootstrapping in this context is not employed to determine confidence intervals from MCS to PCE since the Shapley effects from PCE are computed exactly.

Following [41], a single bootstrap sample $\mathcal{X}_{boot}^{(j)} = \{\boldsymbol{\xi}^{(1)}, \ldots, \boldsymbol{\xi}^{(n_b)}\}$, where $j = 1, 2, \ldots, B$, B is the number of bootstrap replications, and n_b is the size of the bootstrap sample, is created by drawing samples with replacement from the original experimental design. The bootstrap sample will likely have identical samples; however, only unique samples are taken. The j-th bootstrap PCE model $\hat{f}_{boot}^{(j)}(\boldsymbol{\xi})$ is then created by using $\mathcal{X}_{boot}^{(j)}$ as the experimental design. The statistics of interest, which are $\tilde{\phi}_1, \ldots, \tilde{\phi}_m$, can be extracted from $\hat{f}_{boot}^{(j)}(\boldsymbol{\xi})$ analytically. By denoting the i-th Shapley effect from the j-th bootstrap sample as $\tilde{\phi}_{boot_i}^{(j)}$, B PCE models from B bootstrap samples (each with independent sampling with replacement) can be constructed to yield the vector of Shapley effects from bootstrap replications, i.e, $\{\tilde{\phi}_{boot_i}^{(1)}, \tilde{\phi}_{boot_i}^{(2)}, \ldots, \tilde{\phi}_{boot_i}^{(B)}\}$. Subsequently, the bootstrap confidence intervals are computed by calculating the percentiles.

In this paper, we set $B = 500$. The construction of 500 PCE models is significantly faster than evaluating the sampling points. PCE has a rapid construction process, even when using sparse algorithms like LAR. It is important to note that the errors introduced by MCS when estimating the PCE-based Shapley effects are eliminated during the creation of the confidence interval from bootstrap resampling. Therefore, bootstrap resampling is solely used to generate confidence intervals that replicate the impact of random sampling.

D. COMPUTATIONAL PROCEDURE

The complete computational procedure to estimate the Shapley effect using PCE and the associated bootstrap confidence interval is summarized in the following:

1) Prepare the experimental design $\mathcal{X}$ and the responses $\boldsymbol{y}$.
2) Build the PCE model $\hat{f}(\boldsymbol{\xi})$ using $\mathcal{X}$ and $\boldsymbol{y}$.
3) Compute the Shapley effects $\boldsymbol{\phi}$ for all input variables using Eq. (39).
4) Generate bootstrap samples $\mathcal{X}_{boot}^{(1)}$, $\mathcal{X}_{boot}^{(2)}$,..., $\mathcal{X}_{boot}^{(B)}$.
5) Construct B bootstrap PCE models $\hat{f}_{boot}^{(1)}(\boldsymbol{\xi})$, $\hat{f}_{boot}^{(2)}(\boldsymbol{\xi})$, ..., $\hat{f}_{boot}^{(B)}(\boldsymbol{\xi})$ and calculate the corresponding Shapley effects for each bootstrap PCE model.
6) Estimate the bootstrap confidence interval of the Shapley effects (e.g., 90% or 95%).

In this paper, we employ a 95% bootstrap confidence interval to assess the uncertainty in the Shapley effects.

IV. NUMERICAL EXPERIMENTS ON AERODYNAMIC PROBLEMS

A. PRELIMINARY EXPERIMENT: ISHIGAMI FUNCTION

Before explaining the results from the aerodynamic problem, a preliminary experiment was performed to compare the exact calculation of Shapley effects from PCE and MCS. The MCS method being used is the algorithm proposed by Goda [31], which provides the confidence interval without the need for resampling (note that the MCS here is applied on the real function and not the PCE model). The Ishigami function was chosen for the preliminary experiment due to its high nonlinear characteristics described as follows:

$$f(\boldsymbol{x}) = \sin(x_1) + a\sin^2(x_2) + bx_3^4\sin(x_1) \tag{43}$$

where $a = 7$, $b = 0.1$, and $\boldsymbol{\Omega} = [-\pi, \pi]^3$. Ishigami function is a highly nonlinear three-dimensional function with a strong interaction between x_1 and x_3. On the other hand, x_2 does not interact with either x_1 or x_3. The analytical total Sobol indices are as follows: $S_{T_1} = 0.5576$, $S_{T_2} = 0.4424$, and $S_{T_3} = 0.2437$. On the other hand, the Shapley effects are as follows: $\phi_1 = 0.4357$, $\phi_2 = 0.4424$, and $\phi_3 = 0.1218$ [31]. The calculation of total Sobol indices and Shapley effects for the Ishigami function returns different rankings of the variables. The total Sobol indices overestimate the effect of x_1 due to the strong interaction between x_1 and x_3. On the other hand, the Shapley effect ranks x_2 higher than x_1. The Shapley effect gives a fair share to x_1 and x_3 for the Ishigami function, owing to the balanced distribution of the interaction effects. This example serves as a first example of how both GSA metrics yield different rankings, which can be substantial in the context of real-world design.

The experiment was performed using PCE with a maximum order of 14 and Sobol sampling with sample sizes varied from $n = 50$ to $n = 250$ in a step of 25. The convergence of RMSE using 100,000 validation samples is shown in Fig. 1, which shows that the error is extremely small, especially for $n \geq 150$.

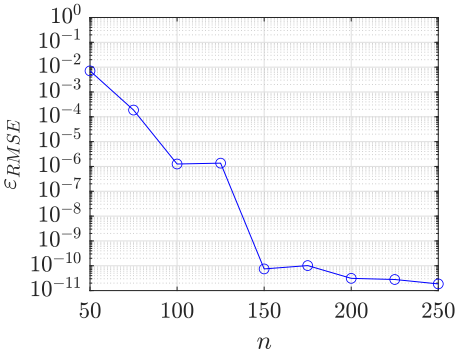

FIGURE 1. The convergence of ϵ_{RMSE} based on a PCE model for the Ishigami function.

The convergence of the Shapley effects for the Ishigami function is shown in Fig. 2. It can be seen that the Shapley effects from PCE eventually converged to those of analytical

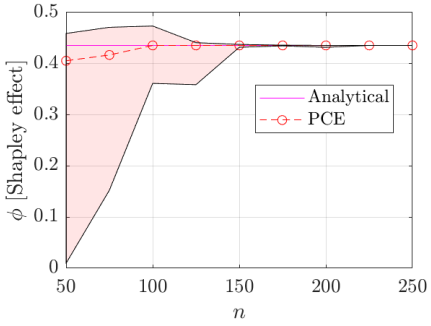

(a) x_1

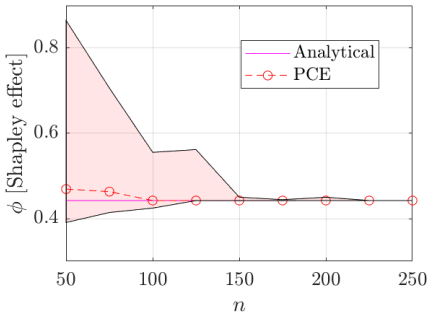

(b) x_2

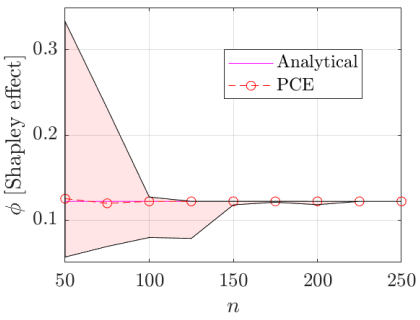

(c) x_3

FIGURE 2. Convergence of the Shapley effects obtained from PCE for the Ishigami function.

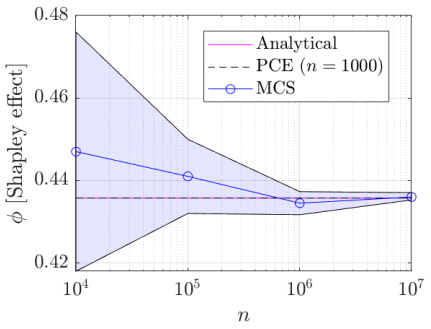

(a) x_1

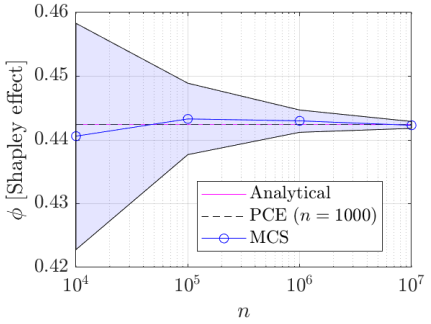

(b) x_2

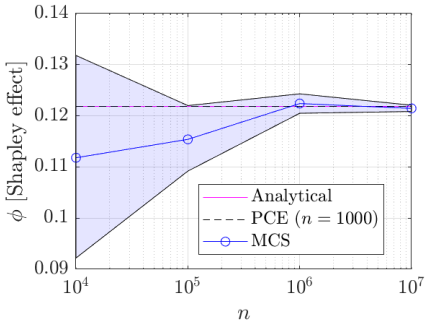

(c) x_3

FIGURE 3. Comparison of the Shapley effects obtained from PCE with $n = 1000$ and MCS applied on the true Ishigami function with $n = 10^4$ to $n = 10^7$. Also shown are the analytical Shapley effects for reference.

values. The result shows that the bootstrap successfully built empirical distributions of the Shapley effects subjected to randomness due to random sampling. The uncertainty for $n = 50$ is especially high; however, the bootstrap confidence interval progressively diminishes with larger sample sizes, resulting in an extremely narrow uncertainty band at $n = 250$.

Let us now consider a scenario in which the Shapley effect is approximated using LAR-PCE with a maximum order of 14 and an experimental design employing $n = 1000$ through Sobol sampling. The resulting PCE is highly accurate, such that the Shapley effects from PCE are extremely close to the analytical value. Even when employing bootstrapping, the PCE-derived confidence interval is remarkably narrow to the extent that it coincides with the analytical values. Fig. 3 presents the analytical and estimated Shapley effects obtained from PCE for $n = 1000$ (represented by straight lines). Further, the Shapley effects derived from MCS are displayed for $n = 10^4$ to 10^7, with the variation shown on a logarithmic scale. We can see that even with a sufficiently large sample size ($n = 10^4$), the confidence interval obtained from MCS is still large due to the extremely nonlinear nature of the Ishigami function. This contrasts PCE, which requires only 150 samples to achieve a sufficiently small confidence interval. A large number of samples is required for MCS to obtain Shapley effect estimates within an acceptably narrow confidence interval. Approximately 10^7 MCS samples are necessary to achieve accurate Shapley effect estimations with sufficiently tight confidence intervals. Using MCS with sample sizes ranging from 10^4 to 10^6 is still insufficient, particularly when sample sizes are limited,

resulting in notably wider confidence intervals. In such cases, it becomes challenging to discern significant differences, especially between x_1 and x_2, due to the high uncertainty associated with the estimations.

The rest of this paper details the application of PCE-based Shapley effects on aerodynamic problems. It is worth noting that implementing the MCS-based Shapley effects on the aerodynamic problems may not be practical due to the following considerations: (1) the cost of evaluating a single evaluation is expensive, which renders the use of MCS infeasible, and (2) the data might come in any form (e.g., Sobol sampling) and it is difficult or not possible to perform more simulations. Thus, for the following aerodynamic problems, we focus the study on the PCE-based Shapley effects and perform a comparison with total Sobol indices. Further, the LOOCV error is computed to assess the accuracy of the PCE on the aerodynamic problems due to relatively limited sampling points.

B. TEST CASE 1: 8-VARIABLE SUBSONIC WING ANALYSIS WITH VORTEX PARTICLE WAKE

The first aerodynamic problem is the GSA of a subsonic wing to investigate the effect of wing twists on aerodynamic performance [42]. The input variables are the twist angle at eight different sections of an untapered wing with NACA 2412 airfoil, varied from -10 to 10 degrees. The analysis evaluates the drag coefficient (C_d) using the vortex particle wake solver available in FLOW5. The problem is solved at a Reynolds number of 11.8×10^6 and a Mach number of 0.5, with a wingspan of 6 m and a chord length of 1 m. The wing is symmetric at the centre, and eight sections are positioned linearly in the spanwise direction from the wing's centre to its tip. The variables number one and eight are the closest to the root and the tip, respectively. Fig. 4 depicts the resulting pressure distribution from the vortex particle wake solver of the nominal geometry and the locations of the eight sections. Sparse PCE models with a maximum order of 3 were constructed using an experimental design with various sample sizes from 50 to 500 in a step of 50, obtained from Sobol sampling. However, we found that the Shapley effects

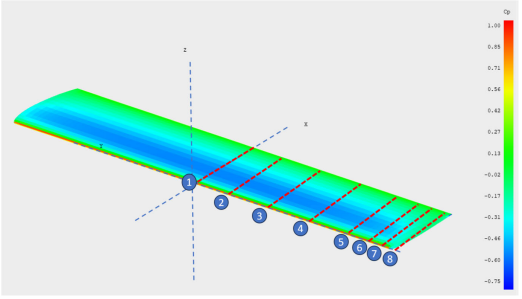

FIGURE 4. The nominal geometry used in the first aerodynamic test problem and the corresponding pressure calculated using the vortex particle wave solver. Also shown are the locations of the eight sections.

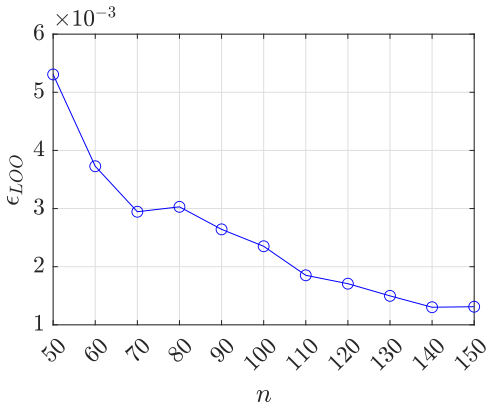

FIGURE 5. The convergence of ϵ_{LOO} for the subsonic wing problem.

already converged at $n = 150$. Thus, we only show the results up to $n = 150$.

Fig. 5 depicts the convergence of the cross-validation error with the sample sizes varied from $n = 50$ to $n = 150$ in a step of 10. The error is small even for the smallest sample size (approximately 10^{-3}), and it reduces further with an increase in sample size. However, as shown later, the case with $n = 50$ still yields a large bootstrap confidence interval.

The problem exhibits a strong interaction, with the sum of all total Sobol indices being equal to 1.751. Additional analysis reveals that three strong interaction terms are present, namely $\xi_1 - \xi_2$ ($S_{12} = 0.172$), $\xi_2 - \xi_3$ ($S_{23} = 0.221$), and $\xi_3 - x_4$ ($S_{34} = 0.1466$). The convergence of Shapley effects for the four most impactful variables is shown in Fig. 6. We have omitted the convergence plots for the remaining four variables to avoid overcrowding the display. From the result, it is interesting to see that the uncertainty band is still wide for $n = 50$ and $n = 60$, especially the former. The Shapley effect values at $n = 50$ are already in close alignment with those at $n = 150$, with a particularly narrow uncertainty band for the latter. Nevertheless, the high uncertainty from the bootstrap confidence interval at $n = 50$ makes it difficult to assess the variable importance. In other words, adding more samples is necessary to increase the confidence. The

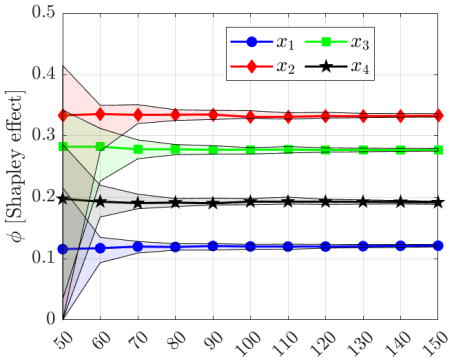

FIGURE 6. Convergence of the Shapley effects of four representative input variables (i.e., x_1, x_2, x_3, and x_4) for the subsonic wing problem.

uncertainty becomes acceptable at $n = 80$, and the band diminishes further when more samples are added. Based on this information, one might consider stopping adding more samples when the bootstrap confidence interval is narrow enough (e.g., at $n = 80$).

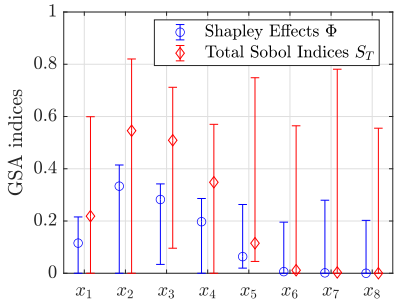

(a) $n = 50$

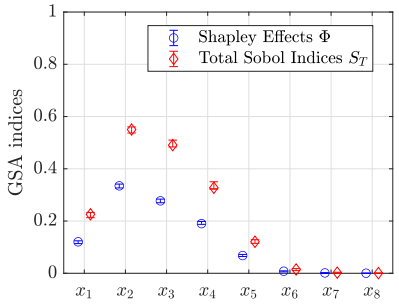

(b) $n = 100$

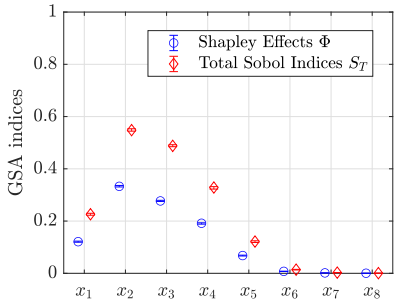

(c) $n = 150$

FIGURE 7. Shapley effects and total Sobol indices results for the subsonic wing problem with $n = 50$, $n = 100$, and $n = 150$.

Figure 7 compares the total Sobol indices and Shapley effects of all variables computed for representative sample sizes ($n = 50$, $n = 100$, and $n = 150$). Despite the significant interaction, both total Sobol indices and Shapley effects produce the same ranking of variables. However, the interpretation of Shapley effects is more meaningful due to their normalization property. The effect of twist on the drag is more pronounced for wing sections closer to the root, except for the section located precisely at the root. Additionally, it is apparent that twisting the wing at the outermost section only slightly affects drag production. From an aerodynamic perspective, twisting a wing at locations close to the root generates more drag because the pressure is higher at these locations. Conversely, twisting the wing precisely at the root has a smaller effect because it only marginally alters the twist at other locations.

At $n = 50$, the Shapley effects still exhibit a relatively high level of uncertainty. The total Sobol indices display even higher uncertainty, leading to interpretation confusion. Notably, the 97.5% quantiles of the total Sobol indices for x_6, x_7, and x_8 are considerably larger than their estimated values due to the overcounting of the interaction terms. This overcounting issue does not occur in the case of Shapley effects, as the weights are allocated fairly to the ANOVA terms. The uncertainty at $n = 50$ is high because the sparse PCE is still sensitive to the changes in the experimental design at such a low sample size. However, the smaller uncertainty in Shapley effects compared to total Sobol indices is advantageous. The confidence intervals' widths become small enough at $n = 100$, even narrower for $n = 150$. Despite having the same variable ranking, there are significant differences between the magnitudes of Shapley effects and Sobol indices.

C. TEST CASE 2: 12-VARIABLE TRANSONIC AIRFOIL WITH UNCERTAIN GEOMETRY

The next case is an inviscid transonic airfoil case with uncertainty in the geometry adopted from Baar et al. [43]. The baseline design is the FFAST airfoil (see Fig. 8) where the output of interest is the drag coefficient (C_d) evaluated using the inviscid solver from SU2 [44]. The ordinate of the airfoil is subjected to uncertainties that are parameterized using disturbance functions. The absis coordinate is denoted as x_c and the disturbance function $f_i(x_c)$, where $i = 1, 2, \ldots, d$ and d is the number of disturbance functions, is defined such that

$$\bar{x}_w = \frac{x_c - c_0}{1 - 2c_0}, x_c \in [c_0, 1 - c_0] \tag{44}$$

$$f_i(x_c) = \sin(\phi \bar{x}_w) \frac{\sin(i\pi \bar{x}_w)}{i} \tag{45}$$

where $c_0 = 0.15$ is selected as the starting point of the disturbance function. There are 12 variables in total assigned to the upper and lower surfaces, with each surface assigned six disturbance functions. The disturbance functions are labeled as up_i and lo_i for the upper and lower surfaces, respectively, where i ranges from 1 to 6. Fig. 8b provides

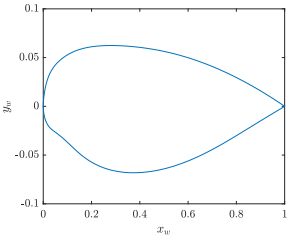

(a) Geometry

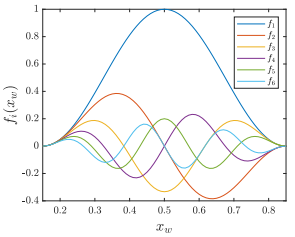

(b) Disturbance functions

FIGURE 8. FFAST airfoil geometry and the six disturbance functions. Note that the disturbance functions are scaled according to the random variable ξ.

a visualization of these six disturbance functions for each surface.

The exact mechanism of how the disturbance function alters the airfoil geometry is defined as follows:

$$\Delta y^{\text{upper}}(x_c) = \sum_{i=1}^{m/2} \xi_i^{\text{upper}} f_i(x_c) \tag{46}$$

$$\Delta y^{\text{lower}}(x_c) = -\sum_{i=1}^{m/2} \xi_i^{\text{lower}} f_i(x_c) \tag{47}$$

where ξ_i are Gaussian random inputs with $\mathbb{E}[\rho(\xi)] = 0$ and $\sigma[\rho(\xi)] = 0.005$ truncated to $\xi \in [-0.0125, 0.0125]$. The case is evaluated at Mach number $M = 0.8$, making it sensitive to the changes in geometry. We denote the ξ^{upper} and ξ^{lower} as *up* and *lo*, respectively, for ease of reading.

The evolution of ϵ_{LOO} for the 12-variable transonic airfoil problem is shown in Fig. 9, in which we varied the sample size from 100 to 900 in a step of 100. It can be seen that the ϵ_{LOO} consistently decreases as the sample size increases, which appears to level off at large sample sizes. Nevertheless, the error is considered acceptable in the context of GSA. What matters most is the inclusion of uncertainty estimates for the calculated Shapley effects, ensuring the ability to draw reliable insights.

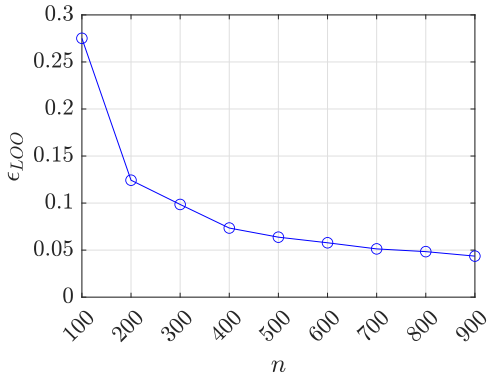

FIGURE 9. The convergence of ϵ_{LOO} for the 12-variable transonic airfoil problem.

Fig. 10 depicts the convergence of four representative input variables (i.e., up_1, up_2, up_5, and lo_3) to show how the band of uncertainty decreases as we increase the sample size. With small sample sizes, especially $n = 100$ and $n = 200$, the uncertainty band is still large, making it difficult to draw solid conclusions regarding the input importance. In such a situation, one might wish to add more samples until the level of uncertainty is small enough for reliable sensitivity analysis. At $n = 600$, the uncertainty begins to reach a more acceptable level, and the distinct impact of each variable becomes more evident. The variables in the problem have strong interactions, with the sum of total Sobol indices calculated from sparse PCE with $n = 900$ being 1.3145. The problem is challenging to approximate

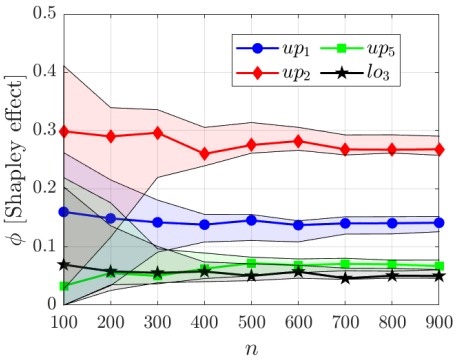

FIGURE 10. Convergence of the Shapley effects of four representative input variables (i.e., up_1, up_2, up_5, and lo_3) for the 12-variable transonic airfoil problem.

using PCE, necessitating a large number of samples to achieve sufficiently narrow confidence intervals.

Fig. 11 displays the calculated GSA metrics and their associated uncertainty estimates for all variables at sample sizes of $n = 300$, $n = 600$, and $n = 900$. The uncertainties are relatively high for $n = 300$, although the differences between the variables are already apparent. An interesting trend can be observed by extracting the GSA indices from the coefficients. The comparison between total Sobol indices and Shapley effects indicates that the two metrics agree on the ranking of the first four most important variables, namely up_2, up_4, up_1, and up_3 based on the magnitude of the indices. However, there is a discrepancy in the interpretation of the fifth most important variable. According to total Sobol indices, up_5 is more important, while Shapley effects suggest that lo_2 should be prioritized. This difference in interpretation can be attributed to the fact that total Sobol indices indicate that all upper surface variables are more important than any of the lower surface variables. While total Sobol indices interpretation says that all upper surface variables are more important than all lower surface variables, Shapley effects show that lo_2 is more important than up_5 and up_6. Therefore, according to Shapley effects, to minimize the variance caused by uncertain geometry, the deformation mode of the lower surface represented by lo_2 should be addressed first before considering the high-frequency deformation modes of the upper surface represented by up_5 and up_6.

Notably, the bootstrapped Shapley effects exhibit lower variances than those of total Sobol indices. This observation is intriguing since the total Sobol indices have an unbounded range on the right side (i.e., $S_T \geq 1$). However, this unbounded nature of the total Sobol indices poses a challenge when interpreting the associated uncertainty. Consequently, Shapley effects offer a more natural approach to account for the main effect and interactions, and their lower variances obtained from PCE also provide greater confidence in the precision of the estimated values. It is worth noting that the prediction accuracy of PCE on this problem is not as high as the other problems, where alternative surrogate models may offer higher accuracy. In fact, one potential drawback of the

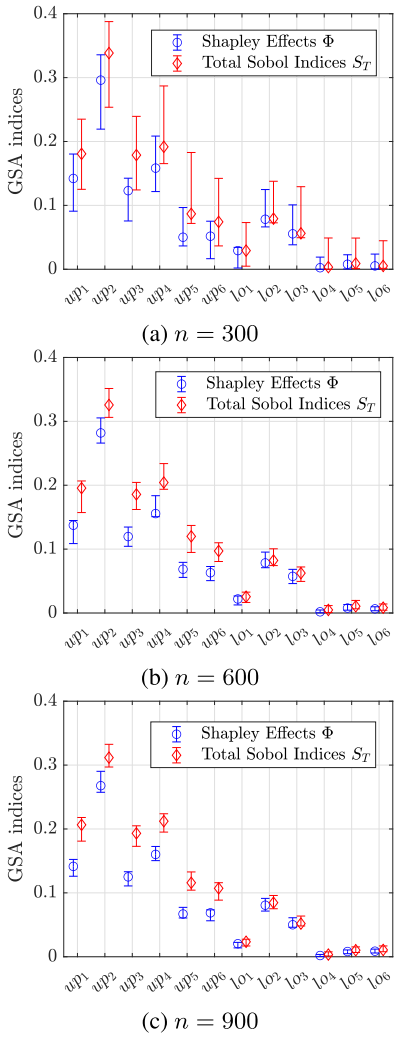

(a) $n = 300$

(b) $n = 600$

(c) $n = 900$

FIGURE 11. Shapley effects and total Sobol indices results for the uncertain transonic airfoil problem with $n = 300$, $n = 600$, and $n = 900$.

fast estimation of PCE-derived Shapley effects stems from the PCE itself, which might be less accurate for some types of problems.

D. TEST CASE 3: FAN-BLADE DESIGN

The fan-blade design adopted from Seshadri et al. with 25 input variables [45] is the next realistic test case. The output of interest is the non-dimensionalized efficiency, which was obtained using a steady-state RANS solver with Spalart-Almaras turbulence closure model with wall function. Each geometry is meshed by 1.75 million mesh elements. Seshadri et al. presented three fan designs, but only the first design (i.e., design A) is utilized in this study. The simulation of blade A is carried out at $Re = 7.8 \times 10^6$, with the pressure and temperature at the bypass outlet equal to $1.005 \times 10^5 N/m^2$ and 288 K, respectively. There are 25 variables that correspond to the modification of dihedral, leading edge (LE) recamber, trailing edge (TE) recamber, sweep, and skew, which are specified at five spanwise locations. For a more comprehensive understanding of this particular case and to view the blade's shape, interested readers are referred to the original paper [45]. To provide an idea of the input-output relationship, Fig. 12 displays a three-dimensional scatter plot of the top three important variables (as per the Shapley effects discussed shortly) with the non-dimensionalized efficiency represented by colour. The plot illustrates that, in general, an increase in x_8, x_9, and x_{10} would result in an increase in efficiency. However, the response is nonlinear, with a quadratic-like shape, as noted by Seshadri et al. [45]. Although not entirely comprehensive, the plot depicted in Fig. 12 provides an approximate mental picture of the input-output relationship.

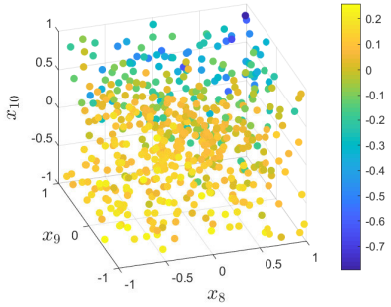

FIGURE 12. A three-dimensional scatter plot of the three most active variables colored by the non-dimensionalized efficiency.

A total of 584 samples are available from the simulation; thus, we use $n = 584$ to construct the sparse PCE with $p_{max} = 3$, yielding $\epsilon_{LOO} = 5.2 \times 10^{-2}$, which was deemed to be sufficiently accurate for GSA purposes. In this particular case, our attention is directed towards examining Shapley effects derived from the sparse PCE only using the complete set of available samples. Employing bootstrapping for a relatively large dimension (specifically, $m = 25$) incurs significant computational costs, so we focus only on using all samples. Moreover, the findings from the previous three problems have already validated the convergence of Shapley effects based on PCE.

The results are shown in Fig. 13. In line with the observation of Seshadri et al., the LE recambering variables are the most important set of variables, followed by TE recambering. The skew variables exhibit a minor contribution to the efficiency, while the other variables are almost non-influential. The interaction appears to be quite strong, with a sum of total Sobol indices equal to 1.2157. The confidence intervals created through bootstrapping are sufficiently narrow, indicating a robust conclusion regarding the variables' importance.

The importance ranking derived from total Sobol indices and Shapley effects differ slightly. To be exact, total Sobol indices assigned the 15th variable (i.e., TE recambering variable) as the third important variable, while Shapley effects place the said variable in number four. Instead, Shapley effects rank the 8th variable, which belongs to

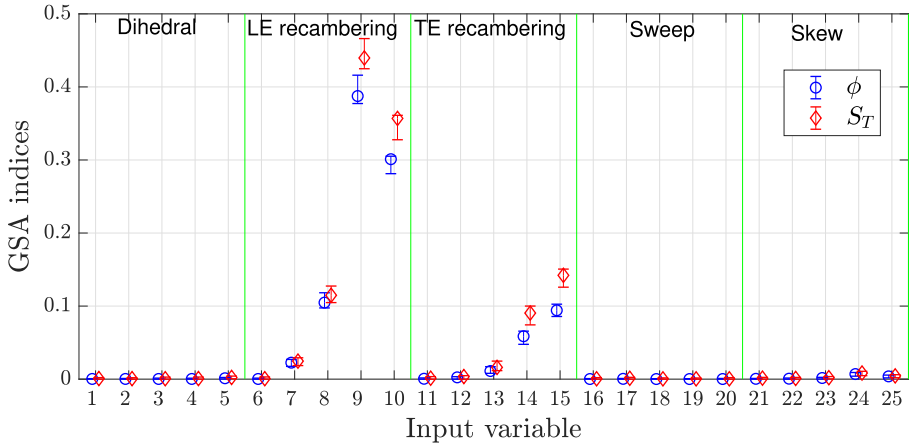

FIGURE 13. GSA of the fan blade design using PCE with $n = 498$.

the LE recambering class, in the third position. Similar to the subsonic wing problem, this discrepancy in ranking may result in a different design strategy for the fan blade. For instance, designers may concentrate exclusively on LE recambering as they are aware that the three most important variables, according to Shapley effects, belong to that particular set.

V. CONCLUSION

The aim of this research paper is to explore the use of sparse PCE for estimating Shapley effects in the context of aerodynamic design exploration. One of the main objectives of aerodynamic design is to identify the relative impact of geometric variables on aerodynamic performance. For instance, if engineers know the variables that contribute the most to aerodynamic efficiency, they can focus on controlling these variables to a greater extent. Shapley effects are considered to be a better alternative to total Sobol indices for GSA, as they have a normalization property, which means that the sum of unnormalized Shapley effects is equal to the function's variance. Once a PCE model is developed, the Shapley effects can be calculated exactly, eliminating uncertainty due to Monte Carlo simulations. Bootstrap estimates the randomness in Shapley effects caused by random sampling, which is now accelerated thanks to the exact calculation from PCE.

To demonstrate the usefulness of Shapley effects, the research focuses on three aerodynamic problems with strong interactions between input variables. The confidence interval is a critical aspect as it provides analysts with information about the uncertainties in Shapley effect predictions. The cost of estimating Shapley effects from PCE is virtually equivalent to that of Sobol indices, as both are derived from PCE coefficients. Hence, the bulk of computational cost comes from constructing the PCE model. Using PCE-based Shapley effects, aerodynamic designers can obtain fast insight into the global sensitivity of the design variables, allowing more efficient and informed decision-making in the design process. This expeditious analysis facilitates the identification of critical variables and informs design adjustments without the computational burdens associated with alternative methods.

The results of our study reveal several important trends. Firstly, we demonstrate that PCE can be utilized to estimate Shapley effects rapidly. Secondly, our findings indicate that total Sobol indices and Shapley effects can produce different importance rankings. However, using Shapley effects is more natural in considering interaction terms, making their results more logical and easier to interpret. In the case of the transonic airfoil with uncertain geometry and fan blade design, the use of Shapley effects results in a distinct ranking when compared to Sobol indices. This disparity may lead to a distinct approach for design or variance minimization concerning uncertainty. Thirdly, the confidence intervals for Shapley effects are lower than those of total Sobol indices, which is particularly significant when the sample size is small. Finally, the uncertainty associated with total Sobol indices is higher than that of Shapley effects, mainly due to the overcounting of interaction terms. As a side note, although fast estimation of Shapley effects from PCE is desirable given a sufficiently accurate approximation, users should be careful with certain classes of problems, e.g., when a discontinuity is present in the input-output relationship. The Shapley effects derived from PCE might be inaccurate and give false insight in such a scenario.

In future studies, the adoption of a Bayesian form of PCE could yield additional advantages, as no further bootstrap procedures are required to construct confidence intervals resulting from random sampling. Moreover, we are intrigued by the possibility of obtaining the analytical formula of Shapley effects from kernel-based models, such as Kriging and support vector regression. In the context of aerodynamic optimization, one promising research direction is to investigate the information obtained from Shapley effects-based GSA for real-world design optimization. For instance, exploring the potential of Shapley effects to reduce

the dimensionality of geometrical design variables to improve efficiency in optimization. Finally, it is interesting to explore the potential utility of Shapley effects within a dynamic system, wherein the sensitivity of input variables and their interactions change over time.

REFERENCES

[1] S. Obayashi, S. Jeong, K. Chiba, and H. Morino, "Multi-objective design exploration and its application to regional-jet wing design," *Trans. Jpn. Soc. Aeronaut. Space Sci.*, vol. 50, no. 167, pp. 1–8, 2007.

[2] S. Obayashi, S.-K. Jeong, K. Shimoyama, K. Chiba, and H. Morino, "Multi-objective design exploration and its applications," *Int. J. Aeronaut. Space Sci.*, vol. 11, no. 4, pp. 247–265, Dec. 2010.

[3] S. Lo Piano, F. Ferretti, A. Puy, D. Albrecht, and A. Saltelli, "Variance-based sensitivity analysis: The quest for better estimators and designs between explorativity and economy," *Rel. Eng. Syst. Saf.*, vol. 206, Feb. 2021, Art. no. 107300.

[4] S. Kucherenko, M. Rodriguez-Fernandez, C. Pantelides, and N. Shah, "Monte Carlo evaluation of derivative-based global sensitivity measures," *Rel. Eng. Syst. Saf.*, vol. 94, no. 7, pp. 1135–1148, 2009.

[5] P. G. Constantine and P. Diaz, "Global sensitivity metrics from active subspaces," *Rel. Eng. Syst. Saf.*, vol. 162, pp. 1–13, Jun. 2017.

[6] Z. Wu, W. Wang, D. Wang, K. Zhao, and W. Zhang, "Global sensitivity analysis using orthogonal augmented radial basis function," *Rel. Eng. Syst. Saf.*, vol. 185, pp. 291–302, May 2019.

[7] P. Wang, Z. Lu, and Z. Tang, "An application of the Kriging method in global sensitivity analysis with parameter uncertainty," *Appl. Math. Model.*, vol. 37, no. 9, pp. 6543–6555, May 2013.

[8] P. Kersaudy, B. Sudret, N. Varsier, O. Picon, and J. Wiart, "A new surrogate modeling technique combining Kriging and polynomial chaos expansions—Application to uncertainty analysis in computational dosimetry," *J. Comput. Phys.*, vol. 286, pp. 103–117, Apr. 2015.

[9] K. Cheng, Z. Lu, Y. Zhou, Y. Shi, and Y. Wei, "Global sensitivity analysis using support vector regression," *Appl. Math. Model.*, vol. 49, pp. 587–598, Sep. 2017.

[10] H. Ma, E.-P. Li, A. C. Cangellaris, and X. Chen, "Support vector regression-based active subspace (SVR-AS) modeling of high-speed links for fast and accurate sensitivity analysis," *IEEE Access*, vol. 8, pp. 74339–74348, 2020.

[11] A. Antoniadis, S. Lambert-Lacroix, and J.-M. Poggi, "Random forests for global sensitivity analysis: A selective review," *Rel. Eng. Syst. Saf.*, vol. 206, Feb. 2021, Art. no. 107312.

[12] B. Sudret, "Global sensitivity analysis using polynomial chaos expansions," *Rel. Eng. Syst. Saf.*, vol. 93, no. 7, pp. 964–979, Jul. 2008.

[13] Q. Shao, A. Younes, M. Fahs, and T. A. Mara, "Bayesian sparse polynomial chaos expansion for global sensitivity analysis," *Comput. Methods Appl. Mech. Eng.*, vol. 318, pp. 474–496, May 2017.

[14] I. M. Sobol, "Global sensitivity indices for nonlinear mathematical models and their Monte Carlo estimates," *Math. Comput. Simul.*, vol. 55, nos. 1–3, pp. 271–280, Feb. 2001.

[15] Y. Yang, L. Chen, Y. Xiong, S. Li, and X. Meng, "Global sensitivity analysis based on BP neural network for thermal design parameters," *J. Thermophys. Heat Transf.*, vol. 35, no. 1, pp. 187–199, Jan. 2021.

[16] L. Hu, J. Zhang, Y. Xiang, and W. Wang, "Neural networks-based aerodynamic data modeling: A comprehensive review," *IEEE Access*, vol. 8, pp. 90805–90823, 2020.

[17] N. Lüthen, S. Marelli, and B. Sudret, "Sparse polynomial chaos expansions: Literature survey and benchmark," *SIAM/ASA J. Uncertainty Quantification*, vol. 9, no. 2, pp. 593–649, Jan. 2021.

[18] K. Cheng, Z. Lu, C. Ling, and S. Zhou, "Surrogate-assisted global sensitivity analysis: An overview," *Struct. Multidisciplinary Optim.*, vol. 61, no. 3, pp. 1187–1213, Mar. 2020.

[19] V. Raul and L. Leifsson, "Surrogate-based aerodynamic shape optimization for delaying airfoil dynamic stall using Kriging regression and infill criteria," *Aerosp. Sci. Technol.*, vol. 111, Apr. 2021, Art. no. 106555.

[20] C. Fan, R. A. Adjei, Y. Wu, and A. Wang, "Parametric study on the aerodynamic performance of a ducted-fan rotor using free-form method," *Aerosp. Sci. Technol.*, vol. 101, Jun. 2020, Art. no. 105842.

[21] M. J. Candon and H. Ogawa, "Numerical analysis and design optimization of supersonic after-burning with strut fuel injectors for scramjet engines," *Acta Astronautica*, vol. 147, pp. 281–296, Jun. 2018.

[22] P. M. M. A. Siddique and L. P. Raj, "Sensitivity analysis of geometric parameters on the aerodynamic performance of a multi-element airfoil," *Aerosp. Sci. Technol.*, vol. 132, Jan. 2023, Art. no. 108074.

[23] N. Mourousias, A. García-Gutiérrez, A. Malim, D. D. Fernández, B. G. Marinus, and M. C. Runacres, "Uncertainty quantification study of the aerodynamic performance of high-altitude propellers," *Aerosp. Sci. Technol.*, vol. 133, Feb. 2023, Art. no. 108108.

[24] J. Wang, B. Wang, H. Yang, Z. Sun, K. Zhou, and X. Zheng, "Compressor geometric uncertainty quantification under conditions from near choke to near stall," *Chin. J. Aeronaut.*, vol. 36, no. 3, pp. 16–29, Mar. 2023.

[25] X. Wu, W. Zhang, S. Song, and Z. Ye, "Sparse grid-based polynomial chaos expansion for aerodynamics of an airfoil with uncertainties," *Chin. J. Aeronaut.*, vol. 31, no. 5, pp. 997–1011, May 2018.

[26] J. Guo, G. Lin, X. Bu, and H. Li, "Sensitivity analysis of flowfield modeling parameters upon the flow structure and aerodynamics of an opposing jet over a hypersonic blunt body," *Chin. J. Aeronaut.*, vol. 33, no. 1, pp. 161–175, Jan. 2020.

[27] B. V. Stein, E. Raponi, Z. Sadeghi, N. Bouman, R. C. H. J. Van Ham, and T. Bäck, "A comparison of global sensitivity analysis methods for explainable AI with an application in genomic prediction," *IEEE Access*, vol. 10, pp. 103364–103381, 2022.

[28] A. B. Owen, "Sobol' indices and Shapley value," *SIAM/ASA J. Uncertainty Quantification*, vol. 2, no. 1, pp. 245–251, Jan. 2014.

[29] E. Song, B. L. Nelson, and J. Staum, "Shapley effects for global sensitivity analysis: Theory and computation," *SIAM/ASA J. Uncertainty Quantification*, vol. 4, no. 1, pp. 1060–1083, Jan. 2016.

[30] B. Iooss and C. Prieur, "Shapley effects for sensitivity analysis with correlated inputs: Comparisons with sobol'indices, numerical estimation and applications," *Int. J. Uncertainty Quantification*, vol. 9, no. 5, pp. 493–514, 2019.

[31] T. Goda, "A simple algorithm for global sensitivity analysis with Shapley effects," *Rel. Eng. Syst. Saf.*, vol. 213, Sep. 2021, Art. no. 107702.

[32] N. Benoumechiara and K. Elie-Dit-Cosaque, "Shapley effects for sensitivity analysis with dependent inputs: Bootstrap and Kriging-based algorithms," *ESAIM, Proc. Surv.*, vol. 65, pp. 266–293, 2019.

[33] D. Xiu and G. E. Karniadakis, "The wiener-askey polynomial chaos for stochastic differential equations," *SIAM J. Sci. Comput.*, vol. 24, no. 2, pp. 619–644, Jan. 2002.

[34] D. Xiu and G. E. Karniadakis, "Modeling uncertainty in flow simulations via generalized polynomial chaos," *J. Comput. Phys.*, vol. 187, no. 1, pp. 137–167, May 2003.

[35] B. Sudret and C. V. Mai, "Computing derivative-based global sensitivity measures using polynomial chaos expansions," *Rel. Eng. Syst. Saf.*, vol. 134, pp. 241–250, Feb. 2015.

[36] P. S. Palar, L. R. Zuhal, K. Shimoyama, and T. Tsuchiya, "Global sensitivity analysis via multi-fidelity polynomial chaos expansion," *Rel. Eng. Syst. Saf.*, vol. 170, pp. 175–190, Feb. 2018.

[37] R. Ahlfeld, B. Belkouchi, and F. Montomoli, "SAMBA: Sparse approximation of moment-based arbitrary polynomial chaos," *J. Comput. Phys.*, vol. 320, pp. 1–16, Sep. 2016.

[38] E. Torre, S. Marelli, P. Embrechts, and B. Sudret, "Data-driven polynomial chaos expansion for machine learning regression," *J. Comput. Phys.*, vol. 388, pp. 601–623, Jul. 2019.

[39] S. Dubreuil, M. Berveiller, F. Petitjean, and M. Salaün, "Construction of bootstrap confidence intervals on sensitivity indices computed by polynomial chaos expansion," *Rel. Eng. Syst. Saf.*, vol. 121, pp. 263–275, Jan. 2014.

[40] G. Blatman and B. Sudret, "Adaptive sparse polynomial chaos expansion based on least angle regression," *J. Comput. Phys.*, vol. 230, no. 6, pp. 2345–2367, Mar. 2011.

[41] S. Marelli and B. Sudret, "An active-learning algorithm that combines sparse polynomial chaos expansions and bootstrap for structural reliability analysis," *Struct. Saf.*, vol. 75, pp. 67–74, Nov. 2018.

[42] P. S. Palar, L. R. Zuhal, and K. Shimoyama, "Enhancing the explainability of regression-based polynomial chaos expansion by Shapley additive explanations," *Rel. Eng. Syst. Saf.*, vol. 232, Apr. 2023, Art. no. 109045.

[43] J. H. S. de Baar, T. P. Scholcz, and R. P. Dwight, "Exploiting adjoint derivatives in high-dimensional metamodels," *AIAA J.*, vol. 53, no. 5, pp. 1391–1395, May 2015.

[44] F. Palacios, J. Alonso, K. Duraisamy, M. Colonno, J. Hicken, A. Aranake, A. Campos, S. Copeland, T. Economon, A. Lonkar, T. Lukaczyk, and T. Taylor, "Stanford University Unstructured (SU^2): An open-source integrated computational environment for multi-physics simulation and design," in *Proc. 51st AIAA Aerosp. Sci. Meeting Including New Horizons Forum Aerosp. Expo.*, Jan. 2013, p. 287.

[45] P. Seshadri, S. Yuchi, G. T. Parks, and S. Shahpar, "Supporting multi-point fan design with dimension reduction," *Aeronaut. J.*, vol. 124, pp. 1371–1398, Sep. 2020.

PRAMUDITA SATRIA PALAR received the Ph.D. degree in aeronautics and astronautics from The University of Tokyo, Japan. During his Ph.D., he was a Visiting Researcher with the Engineering Design Center, University of Cambridge, U.K. In 2023, he was an Invited Assistant Professor with ISAE-SUPAERO, France. He is currently an Assistant Professor with the Faculty of Mechanical and Aerospace Engineering, Bandung Institute of Technology [Institut Teknologi Bandung (ITB)], Indonesia. Prior to his current position, he was a Research Fellow with the Institute of Fluid Science, Tohoku University, Japan. During his postdoctoral position, he visited the Leiden Institute of Advanced Computer Science, Leiden University, as a Visiting Researcher. His research interests include computationally expensive optimization, surrogate models, statistical and machine learning, uncertainty and sensitivity analysis, and their applications in aerospace and aerodynamic design.

LAVI RIZKI ZUHAL received the B.S. degree in aerospace engineering from the University of Maryland, in 1996, and the M.S. and Ph.D. degrees in aeronautics from the California Institute of Technology, in 1997 and 2001, respectively.

He is currently a Professor with the Faculty of Mechanical and Aerospace Engineering, Bandung Institute of Technology (ITB). His research interests include intersection of fluid mechanics, solid mechanics, and computational science. The main theme of his research is to develop mathematical models for complex systems using data from simulations or experiments. He has used these models to gain a deeper understanding of the fundamental physical phenomena and find optimal solutions to scientific and engineering problems. His research also focuses on developing reliable machine learning models and evolutionary algorithms for multidisciplinary design optimization problems, applicable to a wide range of complex real-world problems.

KOJI SHIMOYAMA (Member, IEEE) received the Ph.D. degree from the Department of Aeronautics and Astronautics, University of Tokyo, Japan, in 2006. Before that, he was a Research Assistant with JAXA, a Research Fellow with Tohoku University, a Visiting Scholar with Stanford University, USA, and an Invited Professor with École Centrale de Lyon, France. He is currently a Professor with the Department of Mechanical Engineering, Kyushu University, Japan. His research interests include multi-objective optimization, Bayesian optimization, and uncertainty quantification for fluid machinery design. He has engaged in collaborations with various industries in Japan, applying evolutionary computation and surrogate models to real-world product design and development.